Soft Matter

PAPER

View Article Online
View Journal | View Issue

Cite this: *Soft Matter*, 2015, 11, 3794

Simulation methods for solvent vapor annealing of block copolymer thin films†

A. F. Hannon,‡[ab] W. Bai,[a] A. Alexander-Katz[a] and C. A. Ross*[a]

Received 7th February 2015,
Accepted 27th March 2015

DOI: 10.1039/c5sm00324e

www.rsc.org/softmatter

Recent progress in modelling the solvent vapor annealing of thin film block copolymers is examined in the context of a self-consistent field theory framework. Key control variables in determining the final microdomain morphologies include swelling ratio or swollen film solvent volume fraction, swollen film thickness, substrate and vapor atmosphere surface energies, effective volume fraction, and effective Flory–Huggins interaction parameter. The regime of solvent vapor annealing studied is where the block copolymer has a high enough Flory–Huggins parameter that ordered structures form during swelling and are then trapped in the system through quenching. Both implicit and explicit consideration of the solvent vapor is considered to distinguish the cases in which solvent vapor leads to a non-bulk morphology. Block-selective solvents are considered based on the experimental systems of polystyrene-*b*-polydimethylsiloxane annealed with toluene and heptane. The results of these simulations are compared with these experiments.

Introduction

Solvent vapor annealing (SVA) has become a leading processing method in producing long range ordered structures in thin film block copolymer (BCP) systems.[1–18]SVA is particularly important for BCPs with high Flory–Huggins interaction parameter χ,[1–3,6–10,19–28] which are of interest for making microdomain patterns with small period but which have high order–disorder transition (ODT) temperatures requiring high annealing temperatures. SVA also enables access to non-bulk morphologies such as spheres or lamellae formed from a bulk-cylindrical BCP.[29] The thin film morphology is governed primarily by χ, degree of polymerization N, BCP minority component volume fraction f,[23,29,30] and surface/confinement effects,[31] but SVA provides additional degrees of freedom based on the fraction of different solvents incorporated, their selectivity with respect to each block, and in thin films, solvent effects on the surface and interface energies.

Although there has been great success with SVA in producing ordered structures from BCPs with high χ,[24,32] the detailed physics of how the ordering takes place is not fully understood and many studies have treated the annealing process as a "black box." Real time monitoring of morphology is typically conducted by measuring film thickness using ellipsometry or spectral reflectometry methods,[33–35] by using *in situ* scattering methods,[25,26] or by atomic force microscopy when there is enough elastic contrast between blocks.[36–38] The detailed final morphology is usually characterized through destructive methods such as scanning electron microscopy or transmission electron microscopy in which samples are etched or stained[39] or nonintrusive scattering methods coupled with inverse data analysis methods.[40,41]

GISAXS (grazing incidence small-angle X-ray scattering) studies have characterized the average morphology as a function of annealing time for several BCP systems.[25,42–46] These experiments showed that ordering began during the swelling stages of the thin film and that the final structures were independent of the casting method. If films are swollen too much or if the BCP has a low χ, the order is lost at a critical swelling thickness during the anneal as the system exceeds the ODT.[45,46] In these cases ordered structures reappear during quenching and are highly dependent on the quench dynamics. However, if the system is quenched from an ordered state, little lateral (in-plane) shrinkage is observed and the film collapses in the out-of-plane direction.[46] This implies that the ordered structures formed in the swelled state are essentially preserved apart from an out-of-plane contraction as the solvent escapes. Thus the morphologies formed during SVA are a function of solvent removal rate, swollen solvent concentration, and swollen film thickness, but not the original as cast film morphology.[43]

These experimental results set the stage for trying to model the systems in a realistic manner. Previous attempts at modelling

[a] *Department of Materials Science and Engineering, Massachusetts Institute of Technology, 77 Massachusetts Avenue, Cambridge, Massachusetts 02139, USA. E-mail: caross@mit.edu*
[b] *Now at Materials Science and Engineering Division, National Institute of Standards and Technology, 100 Bureau Drive, Gaithersburg, MD 20899, USA*

† Electronic supplementary information (ESI) available: Experimental details, SCFT modelling details, effective fraction f_{eff} fit details, explicit and implicit model comparison, and additional simulation results. See DOI: 10.1039/c5sm00324e

‡ Current address: Materials Science and Engineering Division, National Institute of Standards and Technology, 100 Bureau Drive, Gaithersburg, MD 20899, USA.

solvent annealed systems have focused on trying to find the final state of the system assuming equilibrium conditions are reached.[47–57] These models have considered solvent either implicitly by using effective χ and volume fraction f parameters that are a function of the solvent incorporated into the system, or explicitly by using a separate partition function for selective solvent species in addition to the polymer partition function. The models correspond to solvent annealed films where ordering occurs during swelling, thus the morphologies found represent structures "frozen" from the swollen state in the final quenched state. More recently, dynamic simulations have been attempted starting with a disordered mixture of neutral solvent and BCP with ordering arising from the assumed quench dynamics imposed on the system.[58] There have also been attempts at modelling the full SVA process starting with a dry disordered film and including solvent in a particle based model.[59] General approaches to dynamical methods have also been suggested.[60]

In this study, we present an overview of the current theoretical framework in understanding the physical process of SVA in light of the recent *in situ* experimental progress with GISAXS and advances in modelling techniques. This framework is then applied to self-consistent field theory (SCFT) simulations with solvent modeled both implicitly and explicitly.

Methods

A. Experimental basis

In SVA experiments, thin films of a BCP are placed in a chamber with a solvent atmosphere. This atmosphere can either be from a liquid reservoir near the sample[61,62] or from a controlled flow of vapor and inert gas into the chamber.[6–8,24,33,63–66] The solvents used can be neutral or selectively preferential to the different blocks in the BCP.[12] The morphologies formed in these thin films can be varied by controlling the vapor pressures and ratio of selective solvents, and often differ qualitatively from the bulk morphology.[24,33,61,67–69] The morphology can even be changed reversibly upon further annealing in solvents with different selectivity.[24,32,70] The solvent plasticizes the film[71–74] raising its diffusivity and allowing ordering to occur even at ambient temperature. During SVA, the film thickness can swell to several times the initial thickness depending upon the solvent and its vapor pressure. SVA is effective both for thick films (*i.e.* with thickness many times L_0, the natural periodicity of microdomains in the BCP) and for films with thickness of $\approx L_0$ which form a monolayer of microdomains. The greatest level of control over the solvent environment is obtained from a continuous flow SVA process where solvent vapor of known composition flows through the sample chamber.[33,34] Terracing (formation of holes and islands on the film surface) can occur for morphologies with in-plane orientation,[75–77] but this is minimized by ensuring that the swelled film thickness is commensurate with the domain spacing.

The model presented here is based on data obtained from thin films of two different molecular weight polystyrene-*b*-polydimethylsiloxane (PS-PDMS) BCPs as well as homopolymer PS and PDMS thin films solvent annealed in various ratios of toluene and heptane vapors. These experiments were performed both in a control flow setup as well as a vented open solvent reservoir. Details of these experiments can be found in the ESI† (S1) as well as previous work.[33,35] However, the methodology can be applied to other polymer systems as well.

B. Theoretical framework

In order to apply simulation methodology to SVA in BCP thin film systems, a framework of the major stages during SVA needs to be defined, schematically shown in Fig. 1. The three stages are swelling, annealing, and quenching. An additional pre-stage, casting, describes how the film is deposited, usually by spin coating from a dilute solution. The pre-stage determines initial film thickness D_0, but assuming a thermodynamic equilibrium is reached during annealing, the memory of the as-cast morphology is lost.[46] Swelling refers to the ingress of solvent into the thin film and the resulting increase in film thickness, and quenching or deswelling refers to solvent egress and the resulting decrease in film thickness. The film is usually assumed to collapse in the out-of-plane direction, preserving in-plane microdomains.[45,46] Annealing refers to the diffusion of polymer chains to form ordered structures in the presence of the solvent, and can occur during swelling and quenching.

C. Modelling

Modelling the sequence of SVA stages is complex, especially if the film forms kinetically trapped structures. For films more

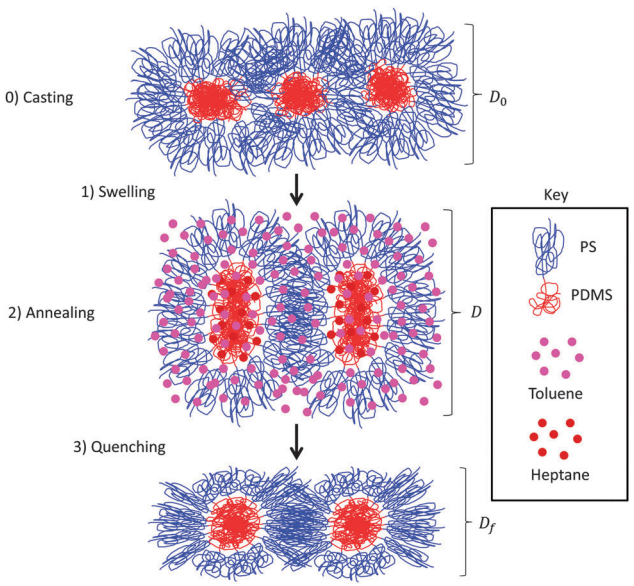

Fig. 1 Schematic diagram showing overall ideal SVA process. Key of structures shown is on the right with blue coils being PS blocks, red coils being PDMS blocks, magenta dots being toluene solvent, and crimson dots being heptane solvent. (0) Casting of thin film of disordered micelles by spin coating or some other deposition method. (1) Swelling of the film occurs once the cast film is placed in solvent vapor atmosphere with film thickness increasing from D_0 to D. (2) Annealing occurs during swelling while the equilibrium film thickness D is reached. (3) Quenching of the film occurs when the solvent atmosphere is removed and the film collapses to a final film thickness D_f. Further annealing may occur during this step.

than a few L_0 thick, the concentration gradient of solvent in the film begins to play an important factor in the dynamics of quenching and can affect the final morphology when quench rates are slow.[9] In the present work, swelled films less than $3L_0$ thick are considered and solvent gradients are neglected. To examine equilibrium morphologies, both an implicit model valid for low to moderate solvent incorporation by volume and a model where the solvent is modeled explicitly using a monoatomic fluid partition function are presented in the framework of SCFT.[78–81] The details of the SCFT simulations used here are given in the ESI† (S2).

The film thickness and effective fraction of BCP in the implicit simulations and fraction of BCP and film thickness in the explicit simulations are determined from the experimental swelling ratio $S_R = D/D_0$, where D is the swollen film thickness before quenching and D_0 is the initial film thickness. An effective χ (or range of χ) is selected to be proportional to the fraction of BCP in the implicit case[42,58,82,83] though this is approximate due to uncertainties in measuring χ, and fluctuation effects.[84] It should be noted the implicit model consists of just the standard BCP model but with effective f and χN parameters based on the incorporated solvents.

Since solvent annealed BCP systems can be thought of as multiple component and species systems, the number of degrees of freedom in the system can become intractable even with a small number of different solvents added to the system. To simplify the simulations, the solvents are treated as effective monomers of the two polymers such that each is completely selective to one of the blocks. This reduces the number of distinct chemical species in the system to two. A neutral solvent would then correspond to equal fractions of both monomers in this model. However, truly neutral solvents would promote a disordered structure, while highly preferential solvents in any ratio would likely promote microphase separation with micelle formation in the dilute polymer limit.

The alternative approach would treat each solvent as its own species, and each solvent added to the system would introduce additional χ parameters for interactions with each block and other solvents already in the system. In general this means for a p species system, there are $\sum_{i=1}^{p}(i-1) = \frac{(p^2-p)}{2}$ Flory–Huggins interaction parameters, *i.e.* 3, 6, 10... interaction parameters for a diBCP with 1, 2, 3... solvents, respectively. Additionally, each solvent has an independent volume fraction parameter. Such an approach quickly becomes intractable, thus we choose to assume the solvents behave analogous to the monomer of the corresponding polymer for which that solvent is selective.

For this assumption that a solvent behaves as a combination of two monomeric species for diBCP systems, an effective χ parameter denoted as χ_{eff} is applied to the system to account for the incorporation of solvent into the system without explicitly having χ parameters for each polymer and/or solvent pair. Previous studies[85] have shown the relationship

$$\chi_{eff} \cong \chi\Phi_{BCP}^{\alpha} = \chi(1 - \Phi_{sol})^{\alpha} \quad (1)$$

to hold for neutral solvents where Φ_{sol} is the volume fraction of solvent in the swollen film and Φ_{BCP} is the volume fraction of BCP in the swollen film (not to be confused with f which refers to the minority component fraction of the BCP). Then

$$\Phi_{sol} = 1 - \Phi_{BCP} = 1 - \frac{1}{S_R} \quad (2)$$

such that $\chi_{eff} \cong \chi S_R^{-\alpha}$. Here α is a constant that is close to 1 in the dry film limit and increases to a value between 1.3 to 1.6 with increasing solvent incorporation.[42] Since most of our experiments have S_R in the range of $1.5 < S_R < 3.0$, χ_{eff} is in the range of $\frac{1}{3^{\alpha}}\chi$ to $\left(\frac{2}{3}\right)^{\alpha}\chi$. If highly selective solvents are used (as is the case of heptane for PDMS[33]), then α can take on values less than 1 or even negative values in eqn (1).[86] In these cases the solvents enhance phase separation between the blocks.

The model also includes an effective N. In the SCFT simulations, the chains are coarse-grained into N_s statistical monomers. Having more N_s segments leads to more accurate simulations, but at the cost of computational time which rises linearly with N_s. For the systems studied here, N_s = 125 which corresponds to $0.25N$ for a 45.5 kg mol^{-1} f = 0.33 PS-PDMS and to $0.15N$ for a 75.5 kg mol^{-1} PS-PDMS with f = 0.41. Length scales in the simulations are determined from $R_g = \lambda\sqrt{N}/\sqrt{6}$ which is then related to L_0 of the BCP features. Here λ is the effective statistical monomer length which is $\sim$0.56 nm in real units as an average for PS and PDMS.[78] L_0 is then given as $L_0 \cong \lambda N^{2/3}\chi^{1/6} \cong \sqrt{6}R_g(\chi N)^{1/6}$ in the high χN limit.[29] To facilitate comparisons, the dimensions of features are normalized to L_0. In principle L_0 itself depends on the solvent incorporation, but this dependence can be relegated into the effective χ and N parameters and how those parameters depend on the incorporated solvent fraction Φ_{sol}.

i. Implicit model. The effective volume fraction f_{eff} is selected such that any incorporated solvent selective to the minority component adds to this effective fraction. This assumption is valid as long as the system remains microphase-separated upon adding solvent. Here we consider a model system with a BCP with minority component A, majority component B, and selective solvents A_{sol} and B_{sol}, respectively. Using the convention that the volume fraction f refers to the minority component A in the BCP, the effective fraction of the A component in a swollen film is

$$f_{eff} = f\Phi_{BCP} + \xi_{A,sol}\Phi_{sol} = fS_R^{-1} + \xi_{A,sol}(1 - S_R^{-1}) \quad (3)$$

where $\xi_{A,sol}$ is the fraction of the total solvent in the film that is A-selective, and $\xi_{A,sol} + \xi_{B,sol} = 1$.

To describe solvents that are not fully selective to either block, such as toluene and heptane in PS-PDMS (heptane is highly preferential to PDMS whereas toluene is preferential to PS but also soluble in PDMS), a "selectivity fit" using β selectivity parameters is constructed which expresses $\xi_{A,sol}$ as a linear combination of the fractions of toluene and heptane that swell only the A-block (PDMS), *i.e.*

$$\xi_{A,sol} = \beta_{tol}\theta_{tol} + \beta_{hept}\theta_{hept} \quad (4)$$

where $\theta_{tol} + \theta_{hept} = 1$ represents the respective fractions in the liquid solvent mixture from which the vapor is produced.

β_{tol} and β_{hept} are the selectivity fit factors for a given solvent mixture, and allow the experiment, in which a solvent vapor consisting of two partially selective solvents is produced from a liquid solvent mixture, to be mapped onto the model, in which the solvent vapor is treated as a combination of fully-selective solvents.

Fit parameters were found from a previous study of the swelling behavior of PS, PDMS, and PS-PDMS thin films in mixed solvent vapors.[33] The fit parameters were: $\beta_{hept} \cong 1$ for all values of θ_{tol},$\beta_{tol} \cong 0$ for $\theta_{tol} < 0.7$, and β_{tol} increased linearly toward a value of 0.25 as θ_{tol} increased to 1. This represents the high selectivity of heptane to the PDMS block for any solvent mixture, whereas toluene is highly selective to the PS block, but starts to enter the PDMS as the solution becomes toluene-rich. Details of these fits are found in the ESI† (S3), but we point out that the data used to generate the fits was obtained from a continuous flow SVA system in which the solvent vapor was produced by bubbling nitrogen through liquid toluene and liquid heptane and mixing the resulting vapors in different proportions. The fits may differ for a system where the vapor is produced from a liquid solvent mixture due to the non-ideality of the toluene–heptane mixture.

Using these fit parameters, the range of f_{eff} accessible for a given PS-PDMS BCP can be calculated for different solvent fractions present and swelling ratios S_R, and the microdomain morphologies then determined. Whether the BCP will still be microphase-separated in the swollen state can be estimated assuming $\chi_{eff}N \geq 10.5$ for microphase-separation to occur.[29,30] Plots of the accessible range of f_{eff} for two PS-PDMS BCPs with molecular weights 45.5 kg mol^{-1} and 75.5 kg mol^{-1} and $f = 0.33$ and $f = 0.41$, respectively, at three swelling ratios are shown in Fig. 2. At these swelling ratios f_{eff} can theoretically cover a range of ~0.2 to 0.7, *i.e.* the swollen BCP thin film could form spherical, cylindrical, gyroid or lamellar structures depending on the solvent mixture used. Moreover, the range of f_{eff} increases with swelling ratio.

These calculations allow a solvent mixture to be determined which is effectively neutral to the two blocks such that $f_{eff} = f$. For $f = 0.33$ this occurs at $\theta_{tol} = 0.66$ (2 to 1 volume ratio of toluene to heptane) and for $f = 0.41$ this occurs at $\theta_{tol} = 0.6$ (3 to 2 toluene to heptane). Also, taking $\alpha = 1$, $\chi_{PS\text{-}PDMS} = 0.14$ at room temperature[87] (other work gives $\chi_{PS\text{-}PDMS}$ as high as 0.27), and $N = 495$ and $N = 847$ for the two different BCPs, $\chi_{eff}N$ exceeds 10.5 for $S_R \leq 6.6$ and $S_R \leq 11.3$ for the two respective N. These rather large S_R are many times greater than the experimental swelling ratios meaning these systems should not disorder upon swelling. Thus implicit simulations should be valid to model the PS-PDMS/toluene–heptane experiments.

ii. Explicit model. In the case of explicit modelling, the SCFT framework used must be modified slightly to treat solvents as explicit species. The main alteration in the theory is the addition of a solvent partition function Q_{sol} in addition to the single chain BCP partition function Q_{BCP}.[80,81,88] Explicit modelling must be used if there is a large quantity of solvent in the system or when χN is so low that upon swelling the film could pass through the ODT. Q_{sol} is given as

$$Q_{sol} = \int d\vec{\mathbf{r}} e^{\Omega_{sol}(\vec{\mathbf{r}})} \quad (5)$$

where $Q_{sol}(\vec{\mathbf{r}})$ is the position-dependent chemical potential field for the appropriate selective solvent.

$$H[\Omega_+, \Omega_-] = C\int d\vec{\mathbf{r}}\left((2f-1)\Omega_- + \frac{{\Omega_-}^2}{\chi N} - \Omega_+\right) - V\sum_{\substack{i=BCP,\\ solA,\\ solB}} \ln(Q_i) \quad (6)$$

is the free energy Hamiltonian with the solvent partition function for a system with species A and B.

In this formalism, there are only A and B selective solvent species. In order to model the toluene and heptane system for PS-PDMS for high toluene fractions $\theta_{tol} > 0.7$ where toluene

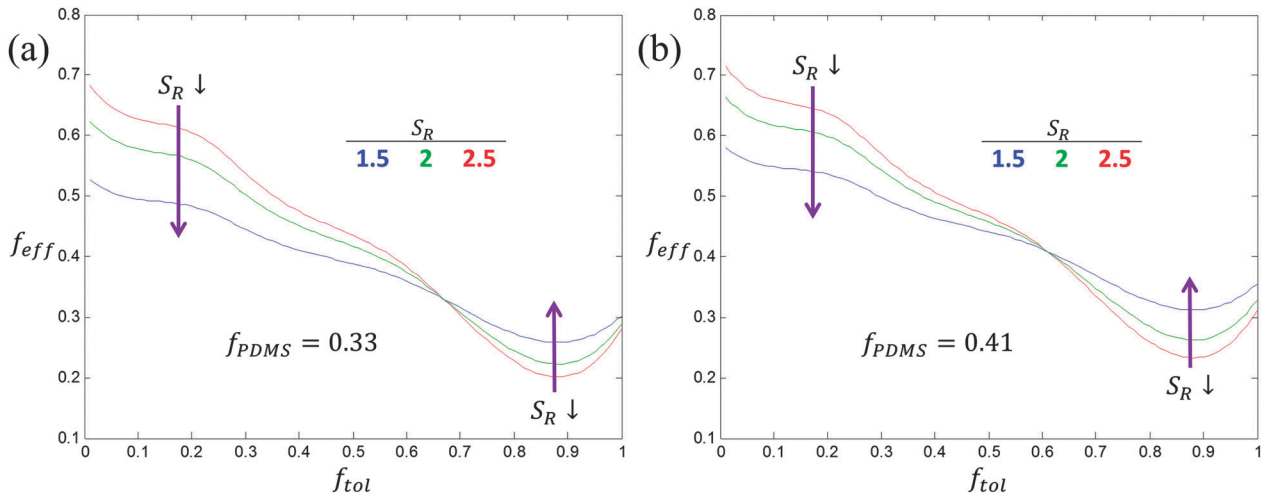

Fig. 2 Plots of f_{eff} using fitted selectivity parameters for toluene and heptane solvents in PS-PDMS BCPs with (a) $f = 0.33$ and (b) $f = 0.41$ for three values of $S_R = 1.5$, 2, and 2.5 shown in blue, green, and red, respectively. A larger range of effective fractions can be obtained at higher swelling ratios. There is a crossover point where $f_{eff} = f$ at (a) $\theta_{tol} = 0.66$ and (b) $\theta_{tol} = 0.6$.

behaves slightly selectively, the toluene fraction in the model needs to be adjusted to account for this selectivity. In other words, in comparing the explicit fractions of selective solvents in simulations with the experimental fractions of solvents, the region of pure B_{sol} is inaccessible experimentally in the PS-PDMS toluene and heptane system since pure toluene will swell both blocks (*i.e.* a solvent purely selective to PS would be needed experimentally to reach this model region). This limitation just means that some of the lower f_{eff} are inaccessible, but could be reached using a solvent with higher preference for PS. This also explains why f_{eff} increases for high θ_{tol} in Fig. 2 rather than continuing to decrease.

In order to calculate normalized densities of A and B, the following equations are evaluated. ϕ_A is the local minority BCP density, ϕ_B is the local majority BCP density, ϕ_{solA} is the local density of A_{sol}, ϕ_B is the density of B_{sol}, Φ_{BCP} is the total fraction of BCP in the system, f_{solA} is the total fraction of A_{sol} in the system, f_{solB} is the total fraction of B_{sol} in the system, $\Phi_{sol} = f_{solA} + f_{solB}$, and q and $q^\dagger$ are the forward and reverse propagators used to calculate the single chain partition function Q_{BCP}.

$$\phi_A(\vec{\mathbf{r}}) = \frac{\Phi_{BCP}}{Q_{BCP}} \int_0^f \mathrm{d}s q^\dagger(\vec{\mathbf{r}}, 1-s, \boldsymbol{\mu})\, q(\vec{\mathbf{r}}, s, \boldsymbol{\mu}) \tag{7}$$

$$\phi_B(\vec{\mathbf{r}}) = \frac{\Phi_{BCP}}{Q_{BCP}} \int_f^1 \mathrm{d}s q^\dagger(\vec{\mathbf{r}}, 1-s, \boldsymbol{\mu})\, q(\vec{\mathbf{r}}, s, \boldsymbol{\mu}) \tag{8}$$

$$\phi_{solA}(\vec{\mathbf{r}}) = \frac{\mathrm{e}^{\Omega_A(\vec{\mathbf{r}})}}{Q_{solA}} f_{solA} \tag{9}$$

$$\phi_{solB}(\vec{\mathbf{r}}) = \frac{\mathrm{e}^{\Omega_B(\vec{\mathbf{r}})}}{Q_{solB}} f_{solB} \tag{10}$$

In these equations Ω_A and Ω_B are defined in terms of Ω_+ and Ω_- as

$$\begin{aligned} \Omega_A &= \Omega_+ + \Omega_- \quad s < f \\ \Omega_B &= \Omega_+ - \Omega_- \quad s \geq f \end{aligned} \tag{11}$$

Upon adding these equations to the SCFT framework, explicit modelling can be performed.

Results and discussion

A. Experimental results

Experimental morphology results for a thin film of 75.5 kg mol^{-1} f = 0.41 are shown in Fig. 3 under a variety of SVA conditions.[35] Four morphologies were observed with $S_R \sim$ 1.5–2.5, monolayer spheres, monolayer cylinders, monolayer perforated lamellae, and monolayer in-plane lamellae, for different solvent mixtures. A range of f_{eff} corresponding to the different experimental solvent ratios is given, calculated from the fitted parameters for β_{tol} (which varies between 0 and 0.25 depending on the solvent mixture) and $\beta_{hept} \cong 1$. This range is given for the cases β_{tol} = 0 and β_{tol} = 0.25. In each of the four different samples in Fig. 3, and in additional cases presented in Table 1, there is a general agreement between the expected morphology for the calculated f_{eff} and the observed morphology.

B. Simulation results

Here we detail the results from simulation studies of both implicit and explicit SVA conditions. Further considerations on how to compare these results with experiments are given in the ESI† (S4).

i. Implicit simulation results. 3D implicit SCFT simulation were performed using parameters that correspond to a 75.5 kg mol^{-1} f = 0.41 PS-PDMS BCP solvent annealed in various mixtures of toluene and heptane.[35] Bulk simulations without solvent were performed initially to determine L_0 for the BCP. L_0 was defined as the spacing of a set of metastable hexagonally packed cylinders. This length scale was chosen since the polymer in the bulk is an equilibrium gyroid phase but gyroids do not form in thin film simulations. L_0 would be related to the gyroid d_{211} spacing such that $d_{211} = \frac{\sqrt{3}}{2} L_0$.[89] Details of the bulk simulations and the determination of L_0 are discussed in the ESI† (S5).

To examine the effects of various solvent ratios on this system, four different effective fractions were chosen and simulations performed over a range of thicknesses. Based on the fitting factors β described above, the four effective volume fractions f_{eff} = 0.25, 0.35, 0.41 and 0.45 correspond to solvent ratios of toluene : heptane that produce morphologies spanning the range from spheres to cylinders to perforated lamellae to lamellae as shown in Table 1.

Periodic boundary conditions were applied in-plane with incommensurate unit cell dimensions of $1.85L_0$ by $1.62L_0$ to avoid biasing the in-plane morphologies. The use of larger simulation cells could also be performed but doing so is more computationally expensive. An effective $(\chi N)_{eff}$ = 18 was chosen as discussed in the ESI† (S5) to best model the approximate value of χ for the swelling conditions examined, though future studies should try to capture χ_{eff} as a function of f_{eff} and S_R explicitly.

To reduce computation time the two surfaces were both chosen to be preferential to the majority block B such that monolayers of spheres, cylinders, perforated lamellae, or lamellae would form without a minority wetting layer, when the film thickness was commensurate with the monolayer thickness. The morphologies are equivalent to those formed for minority-preferential surfaces for films thicker by L_0 (*i.e.* twice each wetting layer thickness of $L_0/2$). The film thickness was varied from $0.5L_0$ up to $1.5L_0$.

Free energy curves with the monolayer morphology highlighted are shown in Fig. 4. The energy has a local minimum when a monolayer of microdomains formed. For the four f_{eff} cases studied, spheres were the monolayer equilibrium morphology for f_{eff} = 0.25, cylinders for f_{eff} = 0.35, perforated lamellae for f_{eff} = 0.41, and in-plane lamellae for f_{eff} = 0.45. Other transitional morphologies were observed at incommensurate thicknesses, and double layer morphologies formed at higher thicknesses. More details are presented in the ESI† (S6).

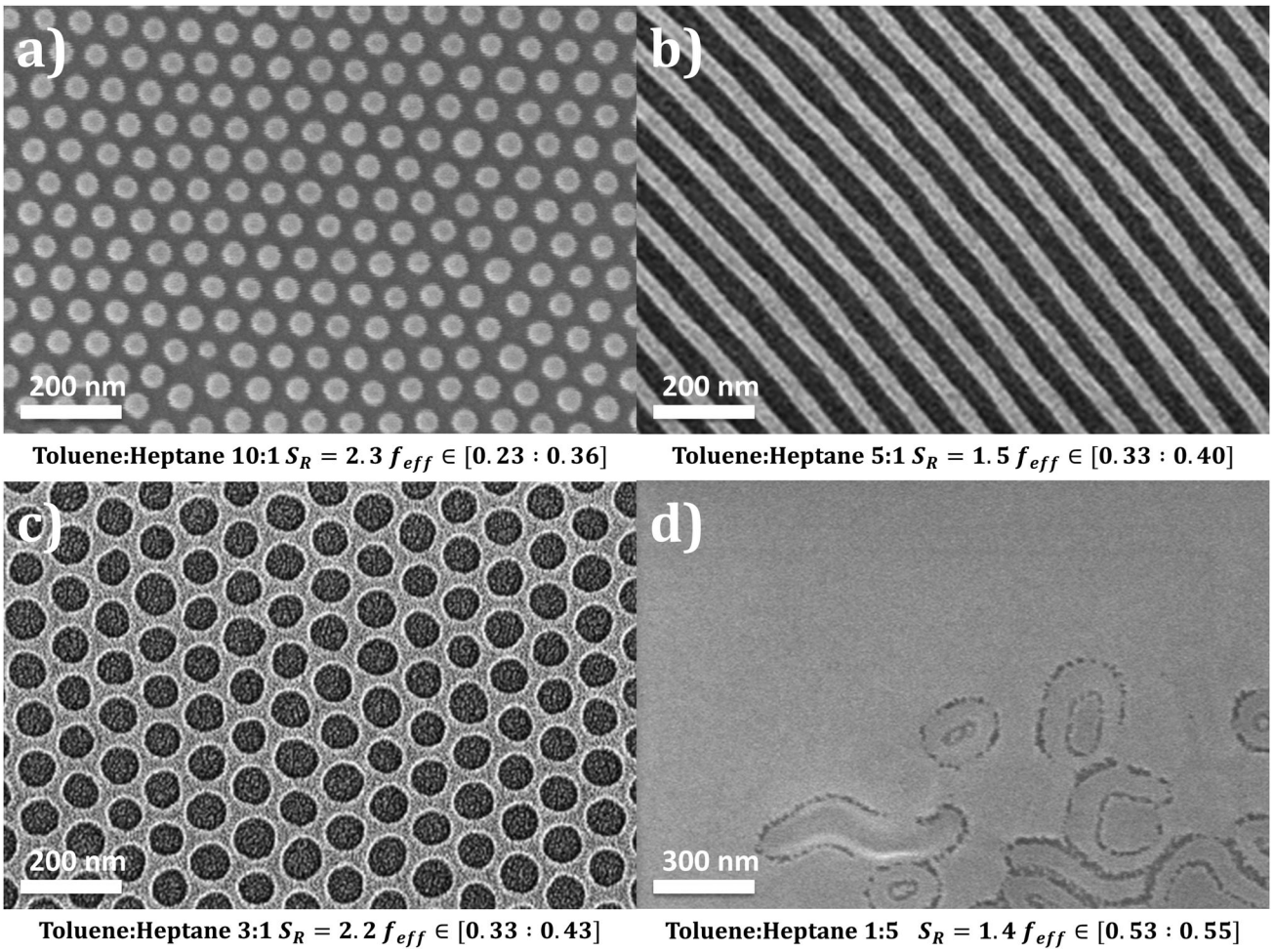

Fig. 3 Scanning electron microscopy images from SVA thin films of a 75.5 kg mol^{-1} PS-PDMS BCP with bulk volume fraction f = 0.415 changing the ratio of toluene : heptane and S_R. The f_{eff} ranges given are calculated based on the range of selectivity of toluene. Lighter regions are PDMS. (a) Spheres. (b) Cylinders. (c) Perforated lamellae. (d) In-plane lamellae.

Table 1 Theoretical f_{eff} ranges using different assumptions about preferentiality of toluene in swelling PDMS domains for different experimental SVA conditions with the corresponding experimentally observed morphologies

Toluene to heptane ratio	θ_{tol}	θ_{hept}	S_R	f_{eff} range	Observed morphology
1 : 0	1.0	0.0	2.5	[0.16 : 0.31]	Spheres
10 : 1	0.91	0.09	2.3	[0.23 : 0.36]	Spheres
5 : 1	0.83	0.17	1.5	[0.33 : 0.40]	Cylinders
4 : 1	0.80	0.20	2.0	[0.31 : 0.41]	Cylinders + perforated lamellae
3 : 1	0.75	0.25	2.2	[0.33 : 0.43]	Perforated lamellae
2.5 : 1	0.71	0.29	1.5	[0.37 : 0.43]	Cylinders + lamellae
1.5 : 1	0.60	0.40	1.3	[0.41 : 0.41]	Perforated lamellae + lamellae
1 : 5	0.17	0.83	1.4	[0.53 : 0.55]	Lamellae

The overall result is that in the implicit model, where a varying solvent ratio is modeled by changing the value of f_{eff}, we predict a range of morphologies which correspond well to those obtained experimentally (spheres, cylinders, perforated lamellae, lamellae at toluene : heptane = 10 : 1, 5 : 1, 3 : 1 and 1 : 5 respectively, Table 1). Additionally, these results are consistent with previous studies of confined thin film morphologies with similar conditions, and a direct comparison of the phase diagram is shown in the ESI† (S7).[90]

ii. Explicit simulation results. Explicit SVA simulations were performed in 2D with f = 0.4 and a fixed χN = 28 with different amounts of solvents with volume fractions f_{solA}, f_{solB}. Simulation cells of size $4L_0$ by $4L_0$ were chosen to be large enough to examine bulk behavior and the fraction of A_{sol} and B_{sol} was varied from 0.00 to 0.60 such that $f_{solA} + f_{solB} \leq 0.60$. The total fraction of BCP is evaluated using the incompressibility constraint that $\Phi_{BCP} + f_{solA} + f_{solB} = 1$. Additionally the effective fraction of A species is simply $f_{eff} = f\Phi_{BCP} + f_{solA}$ where $f_{solA} = \xi_{A,sol}\Phi_{sol}$ and $f_{solB} = \xi_{B,sol}\Phi_{sol}$. Additional 2D simulations over a range of f, χN, f_{solA}, and f_{solB} were also performed to compare the relative phase behavior of the explicit model with the standard BCP phase space. These supplemental simulations and discussion of the results can be found in the ESI† (S8). The main conclusion from those simulations is that $\chi_{eff}(\Phi_{sol})$ depends on the ratio of f_{solA} to f_{solB}, total solvent fraction Φ_{sol}, and the original value of f. Quantifying this exact dependence is an immense task, so two extreme cases were examined in 1D by

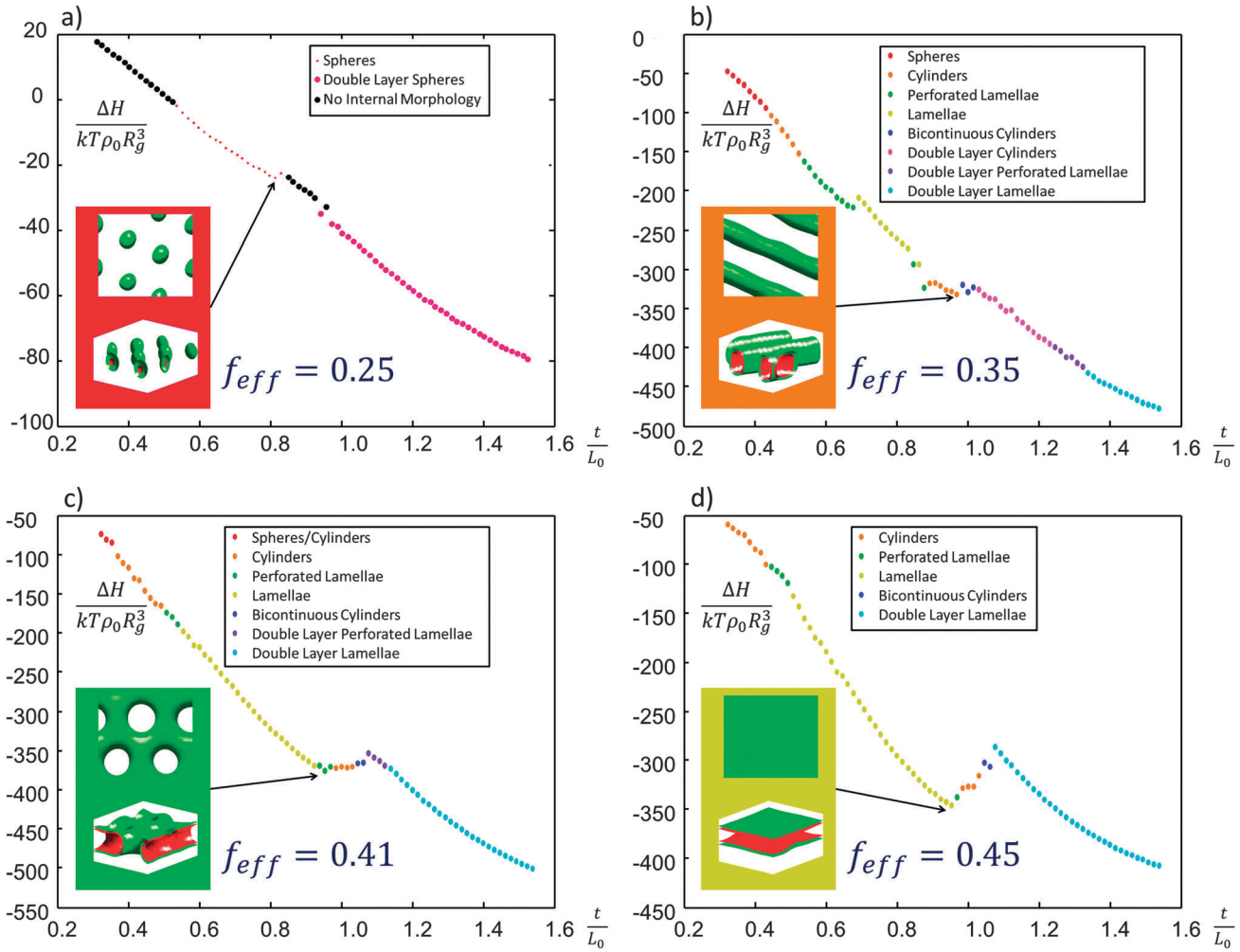

Fig. 4 Plots of the normalized free energy difference ΔH compared to a disordered state for implicit SVA simulations with different f_{eff} as a function of normalized film thickness t/L_0. Inset in each panel are top-down and side-angle views of the monolayer lowest energy structure with green $\phi_A = 0.5$ isosurfaces showing the boundary layer between blocks and the red regions being A rich regions. (a) $f_{eff} = 0.25$, forming spheres as the lowest energy monolayer structure. (b) $f_{eff} = 0.35$, cylinders. (c) $f_{eff} = 0.41$, perforated lamellae. (d) $f_{eff} = 0.45$, in-plane lamellae.

examining how the L_0 of 1D density profiles varied with Φ_{sol} for an $f = 0.5$ copolymer for the cases of only A selective solvent and equal amounts of A and B selective solvents. These results and derived functional dependencies of χ_{eff} on Φ_{sol} are discussed in the ESI† (S9).

As shown in Fig. 5, various phase regions were observed in the simulations depending on the values of f_{solA} and f_{solB}. The 2D bulk morphology with no solvent includes 2D circles (corresponding to through-plane cylinders) and line structures (lamellae) of A. As more f_{solA} is added to the system, the line structures become more dominant and eventually transitions to a perforated A network surrounding circles (or through-plane cylinders of B) and lines of B. As f_{solB} increases, the morphology transitions toward hexagonally close packed circular structures and eventually solvated A-rich micelles. As both A and B solvent fractions are increased, order is eventually lost.

From these results and those in the ESI,† there is a large range of f_{solA} and f_{solB}, up to around $\Phi_{sol} = 0.50$ for ratios of f_{solA} to f_{solB} close to 1 where microphase-separated morphologies are retained without macrophase separation of the solvent from the BCP, with the maximum Φ_{sol} decreasing as the solvent quality approaches pure A or B depending on the exact value of f. The fact that the system can retain ordered structures at such high total solvent fractions gives credence to the ability of implicit simulations to model SVA up to S_R values around 2. A comparison of the density profiles of the two models in 1D is shown in the ESI† (S10) for a case where macrophase segregation did not occur showing these density profiles are qualitatively the same when comparing the total A and B component densities of the explicit model with the A and B densities in the implicit model. However, there are several cases where disorder enters the system or macrophase separation occurs from simply adding more solvent, marking the limitation of implicit simulations. These 2D simulations provide a sense of how the morphology varies with solvent fraction; it is expected in 3D the phase boundaries would be shifted.

Quasi-static simulations were performed in 3D to examine the effect of quenching on the sample morphology. A BCP containing

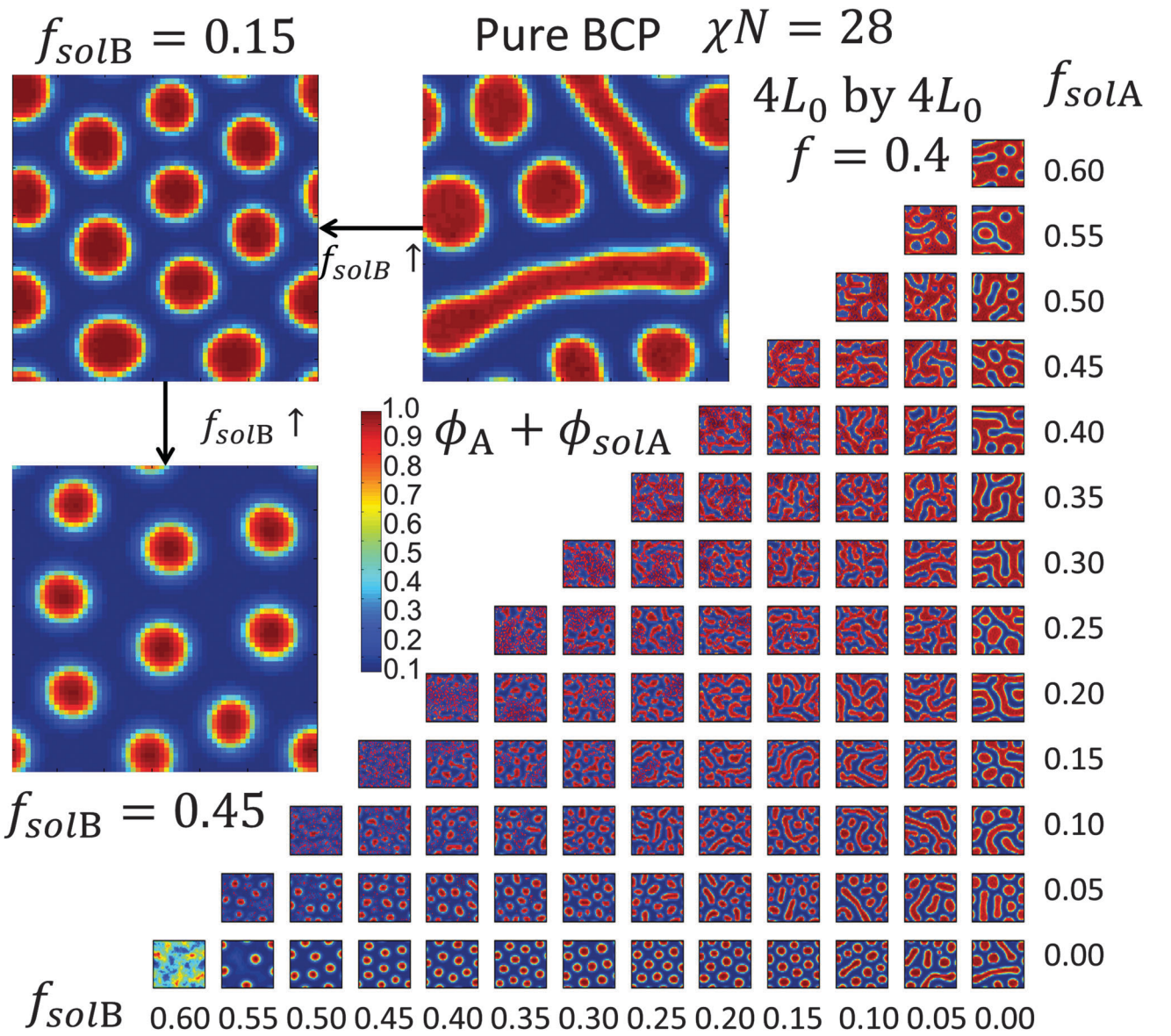

Fig. 5 Minority A species density field maps for 2D simulations of a BCP with f = 0.4 and χN = 28 and various values of explicitly modelled A and B selective solvents. Total A species density is plotted. Inset: zoomed images of pure BCP, f_{solB} = 0.15, and f_{solB} = 0.45 density field maps show the effect of increasing solvent density.

no explicit solvent was first equilibrated to a local saddle point solution. Next, the total unit cell thickness was increased incrementally to a larger swelling ratio by adding solvent, then collapsed back to the original film thickness by removing solvent. Finally the system was re-equilibrated. These simulations yield some information about the structural evolution during swelling and deswelling, but still the simulations only look at local equilibrium states and thus do not determine the kinetic pathway between states since steepest descent methods are still used to relax the fields.

Results using two separate surface wetting cases are shown in Fig. 6. In one case the top and bottom surface energy conditions are both preferential to PDMS (block A), and in the other case only the top surface is A-preferential while the bottom surface is B-preferential. In all these cases the morphologies that formed were in-plane morphologies. The solvent was incorporated such that $f_{solA} = f_{solB}$ and the main variable changed was f reflecting the initial bulk BCP volume fraction. These conditions correspond roughly to neutral solvent, and probe the effect of rapid quenching, unlike the 2D simulations.

As the BCP swelled the A domains increased in diameter but their morphology remained the same, and they shrank upon quenching. For the most part, quenching did not change the swollen morphology but in a few cases of perforated lamellae the swelling/quenching sequence led to a transition to a new morphology. These cases where a phase transition occurred represent either a metastable phase being encountered or a first order phase transition between phases due to the change

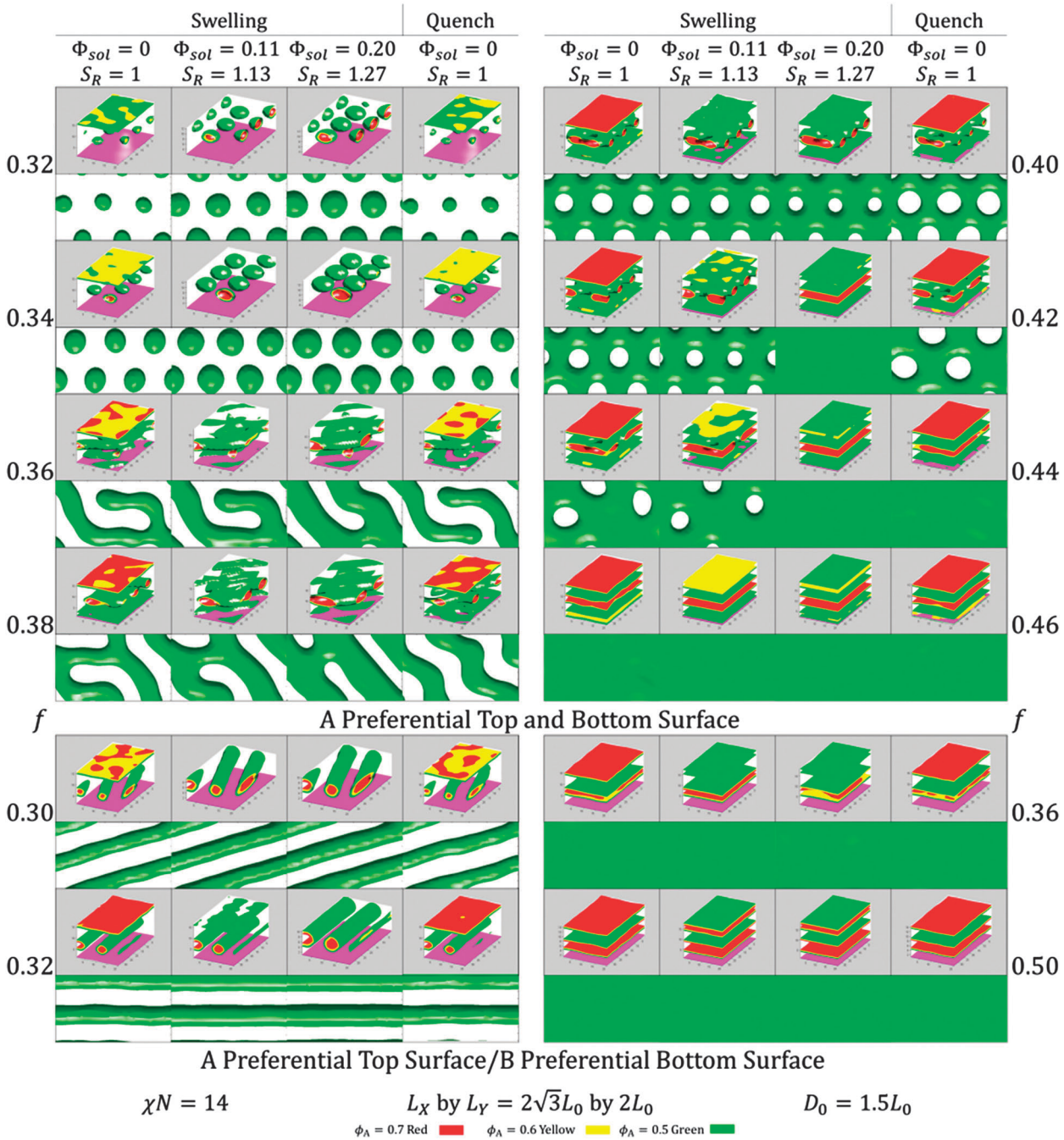

Fig. 6 Quasi-static 3D explicit SVA simulations using different f values. $\chi N = 14$ and the unit cells were commensurate with close-packed features. The initial film thickness was $1.5L_0$. S_R up to 1.27 are shown. Upper panels: top and bottom A-preferential conditions. As f increases hexagonally close packed spheres, cylinders, perforated lamellae, and in-plane lamellae are all observed. Only in the case of perforated lamellae does the morphology change appreciably upon quenching, likely because of metastability of the morphology at the simulated f. Alternatively, this observed behavior may simply be due to the first order phase transition between the equilibrium phases at different solvent fraction conditions. Bottom panels: top A and bottom B preferential conditions. Only cylinders and lamellae were observed for the f examined here, with perforated lamellae being suppressed.

in incorporated solvent fraction. A more comprehensive investigation would examine more thicknesses and solvent ratios, as well as changing χ and adjusting the surface preferentiality with increasing solvent fraction, but the results here indicate that explicit solvent incorporation is a good first step to model morphological changes. Additional quasi-static explicit SVA simulations are detailed in the ESI† (S11).

Conclusions

Both implicit and explicit SCFT simulations provide insight into the physics of SVA. By using effective parameters based on the amount of solvent incorporation, and treating the system as a two species system, predictions of the regimes where different thin film morphologies can be obtained becomes possible.

The modelling was compared to results from PS-PDMS annealed in toluene and heptane vapors, in which the measured selectivity of the solvents to the blocks was used to derive a selectivity fit allowing the system to be mapped onto an idealized model with two fully-selective solvents. Both modelling and experiment show that spherical, cylindrical, perforated lamellar, and lamellar morphologies are obtained by varying the solvent ratio. The simulations and experiments compared here show the potential of SVA to access a wide array of morphologies simply by controlling selective solvent fractions. Future advances will allow the prediction of morphologies formed under a variety of SVA conditions, and the prediction of dynamic annealing paths to understand systems in which the ODT is reached upon swelling.

List of abbreviations, variables and symbols

Abbreviations

SVA	Solvent vapor annealing
BCP	Block copolymer
SCFT	Self-consistent field theory
GISAXS	Grazing incidence small-angle X-ray scattering
PS	Polystyrene
PDMS	Polydimethylsiloxane
ODT	Order–disorder transition

Variables and symbols

χ	Flory–Huggins interaction parameter ''chi''
f	BCP minority component (PDMS in this study) volume fraction
N	Degree of polymerization
D_0	Initial film thickness
D	Swollen film thickness
D_f	Final film thickness after quenching
L_0	Natural BCP microdomain periodicity
S_R	Swelling ratio of swollen film thickness to initial film thickness
p	Number of species in a system
i	Species index
χ_{eff}	Effective χ parameter accounting for solvent incorporation
R_g	Radius of gyration of BCP
Φ_{BCP}	Fraction of swollen thin film that is BCP
Φ_{sol}	Volume fraction of solvent in swollen film
α	Exponent constant relating S_R to χ_{eff}
N_s	Number of statistical chain segments in SCFT model
λ	Effective statistical monomer length ($\sim$2 chemical repeat monomers)
f_{eff}	Volume fraction of minority component (PDMS) plus PDMS/minority component selective solvent present in a swollen film
A	Minority component in implicit model (corresponds to PDMS and toluene & heptane in PDMS)
B	Majority component in implicit model (corresponds to PS and toluene & heptane in PS)
A_{sol}	Solvent selective to A component
B_{sol}	Solvent selective to B component
$\xi_{A,sol}$	Fraction of solvent in film that is A_{sol}
$\xi_{B,sol}$	Fraction of solvent in film that is B_{sol}
β_{tol}	Selectivity fit parameter for toluene
β_{hept}	Selectivity fit parameter for toluene
θ_{tol}	Fraction of solvent in film that is toluene
θ_{hept}	Fraction of solvent in film that is heptane
$\chi_{PS\text{-}PDMS}$	Bulk Flory–Huggins interaction parameter between PS & PDMS
Q_{sol}	Partition function of solvent in SCFT model (Q_{solA} and Q_{solB})
Q_{BCP}	Single chain BCP partition function in SCFT model
$\vec{\mathbf{r}}$	Coordinate vector in SCFT model. Corresponds to real space grid point locations (x,y,z)
H	Hamiltonian in SCFT model that corresponds to the normalized free energy when evaluated with an SCFT chemical potential field solution
Ω_{sol}	Chemical potential field of solvent in SCFT model
Ω_+	Pressure-like chemical potential field in SCFT model
Ω_-	Exchange interaction chemical potential field in SCFT model
Ω_A	Chemical potential field for A component in SCFT model
Ω_B	Chemical potential field for B component in SCFT model
C	Proportionality constant for H in SCFT model that is a function of the polymer density, R_g, and N
V	Volume of unit cell in SCFT calculations
ϕ_A	Normalized density of A polymer in SCFT model
ϕ_B	Normalized density of B polymer in SCFT model
s	Chain coordinate position along the BCP chain (range of 0 to 1 where 0 is the chain head and 1 the chain tail)
q & $q^\dagger$	Forward and reverse partition function propagators, respectively
$\boldsymbol{\mu}$	Total chemical potential field at a given spatial location
ϕ_{solA}	Normalized density of A selective solvent in explicit SCFT model
ϕ_{solB}	Normalized density of B selective solvent in explicit SCFT model
f_{solA}	Fraction of unit cell volume that is A selective solvent in explicit SCFT model
f_{solB}	Fraction of unit cell volume that is B selective solvent in explicit SCFT model
t	Film thickness in implicit SCFT simulations (corresponds to D in experiment)

Acknowledgements

We thank Kevin W. Gotrik for his previous experimental contributions and insights that led to the development of many model details. We thank Professor Apostolos Avgeropoulos and

his research group at the University of Ioannina, Greece for synthesizing the PS-PDMS polymers used in the experimental comparison of the simulations. We gratefully acknowledge financial support from the National Science Foundation award CMMI 1246740, Taiwan Semiconductor Manufacturing Company, Tokyo Electron Limited, and the Semiconductor Research Corporation.

References

1 A. W. Harant and C. N. Bowman, *J. Vac. Sci. Technol., B: Microelectron. Nanometer Struct.*, 2005, **23**, 1615–1621.
2 Y. Xuan, J. Peng, L. Cui, H. Wang, B. Li and Y. Han, *Macromolecules*, 2004, **37**, 7301–7307.
3 S. Kim, R. Briber and A. Karim, *MRS Proc.*, 2006, **961**, 0961.
4 M. Luo and T. H. Epps, *Macromolecules*, 2013, **46**, 7567–7579.
5 C. Sinturel, M. Vayer, M. Morris and M. A. Hillmyer, *Macromolecules*, 2013, **46**, 5399–5415.
6 K. A. Cavicchi and T. P. Russell, *Macromolecules*, 2007, **40**, 1181–1186.
7 J. N. L. Albert, T. D. Bogart, R. L. Lewis, K. L. Beers, M. J. Fasolka, J. B. Hutchison, B. D. Vogt and T. H. Epps, *Nano Lett.*, 2011, **11**, 1351–1357.
8 Y. Tada, H. Yoshida, Y. Ishida, T. Hirai, J. K. Bosworth, E. Dobisz, R. Ruiz, M. Takenaka, T. Hayakawa and H. Hasegawa, *Macromolecules*, 2012, **45**, 292–304.
9 S. H. Kim, M. J. Misner and T. P. Russell, *Adv. Mater.*, 2004, **16**, 2119–2123.
10 J. Peng, D. H. Kim, W. Knoll, Y. Xuan, B. Li and Y. Han, *J. Chem. Phys.*, 2006, **125**, 64702.
11 A. Stenbock-Fermor and A. Knoll, *Macromolecules*, 2014, **47**, 3059–3067.
12 J. D. Cushen, L. Wan, G. Pandav, I. Mitra, G. E. Stein, V. Ganesan, R. Ruiz, C. G. Willson and C. J. Ellison, *J. Polym. Sci., Part B: Polym. Phys.*, 2014, **52**, 36–45.
13 C.-J. Chu, P.-Y. Chung, M.-H. Chi, Y.-H. Kao and J.-T. Chen, *Macromol. Rapid Commun.*, 2014, **35**, 1598–1605.
14 S. W. Hong, D. L. Voronov, D. H. Lee, A. Hexemer, H. A. Padmore, T. Xu and T. P. Russell, *Adv. Mater.*, 2012, **24**, 4278–4283.
15 E. Kim, W. Kim, K. H. Lee, C. A. Ross and J. G. Son, *Adv. Funct. Mater.*, 2014, **24**, 6981–6988.
16 J. M. Kim, Y. Kim, W. I. Park, Y. H. Hur, J. W. Jeong, D. M. Sim, K. M. Baek, J. H. Lee, M.-J. Kim and Y. S. Jung, *Adv. Funct. Mater.*, 2015, **25**, 306–315.
17 P. Mokarian-Tabari, C. Cummins, S. Rasappa, C. Simao, C. M. Sotomayor Torres, J. D. Holmes and M. A. Morris, *Langmuir*, 2014, **30**, 10728–10739.
18 J. Kao, K. Thorkelsson, P. Bai, Z. Zhang, C. Sun and T. Xu, *Nat. Commun.*, 2014, **5**, 4053.
19 M. P. Stoykovich and P. F. Nealey, *Mater. Today*, 2006, **9**, 20–29.
20 S. O. Kim, H. H. Solak, M. P. Stoykovich, N. J. Ferrier, J. J. de Pablo and P. F. Nealey, *Nature*, 2003, **424**, 411–414.
21 R. Ruiz, H. Kang, F. A. Detcheverry, E. Dobisz, D. S. Kercher, T. R. Albrecht, J. J. de Pablo and P. F. Nealey, *Science*, 2008, **321**, 936–939.
22 S. Park, D. H. Lee, J. Xu, B. Kim, S. W. Hong, U. Jeong, T. Xu and T. P. Russell, *Science*, 2009, **323**, 1030–1033.
23 T. Lodge and M. Dalvi, *Phys. Rev. Lett.*, 1995, **75**, 657–660.
24 Y. S. Jung and C. A. Ross, *Adv. Mater.*, 2009, **21**, 2540–2545.
25 M. Y. Paik, J. K. Bosworth, D.-M. Smilges, E. L. Schwartz, X. Andre and C. K. Ober, *Macromolecules*, 2010, **43**, 4253–4260.
26 Z. Di, D. Posselt, D.-M. Smilgies and C. M. Papadakis, *Macromolecules*, 2010, **43**, 418–427.
27 J. Vogelsang, J. Brazard, T. Adachi, J. C. Bolinger and P. F. Barbara, *Angew. Chem., Int. Ed.*, 2011, **50**, 2257–2261.
28 W. A. Phillip, M. A. Hillmyer and E. L. Cussler, *Macromolecules*, 2010, **43**, 7763–7770.
29 F. S. Bates and G. H. Fredrickson, *Annu. Rev. Phys. Chem.*, 1990, **41**, 525–557.
30 L. Leibler, *Macromolecules*, 1980, **13**, 1602–1617.
31 A. Knoll, A. Horvat, K. S. Lyakhova, G. Krausch, G. J. A. Sevink, A. V Zvelindovsky and R. Magerle, *Phys. Rev. Lett.*, 2002, **89**, 035501.
32 Y. S. Jung and C. A. Ross, *Nano Lett.*, 2007, **7**, 2046–2050.
33 K. W. Gotrik, A. F. Hannon, J. G. Son, B. Keller, A. Alexander-Katz and C. A. Ross, *ACS Nano*, 2012, **6**, 8052–8059.
34 K. W. Gotrik and C. A. Ross, *Nano Lett.*, 2013, **13**, 5117–5122.
35 W. Bai, A. F. Hannon, K. W. Gotrik, H. K. Choi, K. Aissou, G. Liontos, K. Ntetsikas, A. Alexander-Katz, A. Avgeropoulos and C. A. Ross, *Macromolecules*, 2014, **47**, 6000–6008.
36 M. van Dijk and R. van den Berg, *Macromolecules*, 1995, **28**, 6773–6778.
37 I. Hamley, S. Connell and S. Collins, *Macromolecules*, 2004, **37**, 5337–5351.
38 S. Kim, M. Misner and T. Xu, *Adv. Mater.*, 2004, **16**, 226–231.
39 M. Park, *Science*, 1997, **276**, 1401–1404.
40 D. F. Sunday, M. R. Hammond, W.-L. Wu, R. J. Kline and G. E. Stein, *J. Micro/Nanolithogr., MEMS, MOEMS*, 2013, **12**, 031103.
41 D. Sunday, M. Hammond, C. Wang, W.-L. Wu, D. M. Delongchamp, M. Tjio, J. Y. Cheng, J. W. Pitera and R. J. Kline, *ACS Nano*, 2014, **8**, 8426–8437.
42 X. Gu, I. Gunkel, A. Hexemer, W. Gu and T. P. Russell, *Adv. Mater.*, 2014, **26**, 273–281.
43 X. Gu, I. Gunkel, A. Hexemer and T. P. Russell, *Colloid Polym. Sci.*, 2014, **292**, 1795–1802.
44 J. Zhang, D. Posselt and D. Smilgies, *Macromolecules*, 2014, **47**, 5711–5718.
45 A. Baruth, M. Seo, C. H. Lin, K. Walster, A. Shankar, M. A. Hillmyer and C. Leighton, *ACS Appl. Mater. Interfaces*, 2014, **6**, 13770–13781.
46 C. Sinturel and D. Grosso, *ACS Appl. Mater. Interfaces*, 2014, **6**, 12146–12152.
47 J. G. Son, J.-B. Chang, K. K. Berggren and C. A. Ross, *Nano Lett.*, 2011, **11**, 5079–5084.
48 J. G. Son, A. F. Hannon, K. W. Gotrik, A. Alexander-Katz and C. A. Ross, *Adv. Mater.*, 2011, **23**, 634–639.

49 J.-B. Chang, J. G. Son, A. F. Hannon, A. Alexander-Katz, C. A. Ross and K. K. Berggren, *ACS Nano*, 2012, **6**, 2071–2077.
50 K. G. A. Tavakkoli, A. F. Hannon, K. W. Gotrik, A. Alexander-Katz, C. A. Ross and K. K. Berggren, *Adv. Mater.*, 2012, **24**, 4249–4254.
51 K. G. A. Tavakkoli, K. W. Gotrik, A. F. Hannon, A. Alexander-Katz, C. A. Ross and K. K. Berggren, *Science*, 2012, **336**, 1294–1298.
52 K. G. A. Tavakkoli, S. M. Nicaise, A. F. Hannon, K. W. Gotrik, A. Alexander-Katz, C. A. Ross and K. K. Berggren, *Small*, 2013, **10**, 493–499.
53 P. Sun, Y. Yin, B. Li, T. Chen, Q. Jin, D. Ding and A.-C. Shi, *J. Chem. Phys.*, 2005, **122**, 204905.
54 Y. Yin, P. Sun, B. Li, T. Chen, Q. Jin, D. Ding and A.-C. Shi, *Macromolecules*, 2007, **40**, 5161–5170.
55 R. Jiang, B. Li, Z. Wang, Y. Yin and A.-C. Shi, *Macromolecules*, 2012, **45**, 4920–4931.
56 J. Xu, Y. Yin, Z. Wang, R. Jiang, B. Li and A.-C. Shi, *J. Chem. Phys.*, 2013, **138**, 114905.
57 F. Léonforte and M. Müller, *Macromolecules*, 2015, **48**, 213–228.
58 S. P. Paradiso, K. T. Delaney, C. J. García-Cervera, H. D. Ceniceros and G. H. Fredrickson, *ACS Macro Lett.*, 2014, **3**, 16–20.
59 S.-M. Hur, G. S. Khaira, A. Ram, M. Mu, P. F. Nealey and J. J. de Pablo, *ACS Macro Lett.*, 2015, **4**, 11–15.
60 M. Müller and J. J. de Pablo, *Annu. Rev. Mater. Res.*, 2013, **43**, 1–34.
61 R. Guo, H. Huang, Y. Chen, Y. Gong, B. Du and T. He, *Macromolecules*, 2008, **41**, 890–900.
62 J. W. Jeong, W. I. Park, M. Kim, C. A. Ross and Y. S. Jung, *Nano Lett.*, 2011, **11**, 4095–4101.
63 T. N. Zwietering, *Chem. Eng. Sci.*, 1959, **11**, 1–15.
64 A. Cholette and L. Cloutier, *Can. J. Chem. Eng.*, 1959, **37**, 105–112.
65 A. Horvat, K. S. Lyakhova, G. J. A. Sevink, A. V Zvelindovsky and R. Magerle, *J. Chem. Phys.*, 2004, **120**, 1117–1126.
66 J. N. L. Albert, W.-S. Young, R. L. Lewis, T. D. Bogart, J. R. Smith and T. H. Epps, *ACS Nano*, 2012, **6**, 459–466.
67 J. Bang, B. J. Kim, G. E. Stein, T. P. Russell, X. Li, J. Wang, E. J. Kramer and C. J. Hawker, *Macromolecules*, 2007, **40**, 7019–7025.
68 J. K. Bosworth, M. Y. Paik, R. Ruiz, E. L. Schwartz, J. Q. Huang, A. W. Ko, D.-M. Smilgies, C. T. Black and C. K. Ober, *ACS Nano*, 2008, **2**, 1396–1402.
69 G. Cui, M. Fujikawa, S. Nagano, M. Sano, H. Takase, T. Miyazaki, S. Sakurai and K. Yamamoto, *Polymer*, 2014, **55**, 1601–1608.
70 J. P. Singer, K. W. Gotrik, J.-H. Lee, S. E. Kooi, C. A. Ross and E. L. Thomas, *Polymer*, 2014, **55**, 1875–1882.
71 K. Mori, H. Hasegawa and T. Hashimoto, *Polymer*, 1990, **31**, 2368–2376.
72 C. M. Hansen, *Hansen Solubility Parameters, A User's Handbook*, CRC Press, Boca Raton, FL, 2000.
73 P. Bahadur and N. V. Sastry, *Principles of Polymer Science*, Alpha Science International, Ltd, Oxford, UK, 2005.
74 H. Elbs and G. Krausch, *Polymer*, 2004, **45**, 7935–7942.
75 G. Coulon, B. Collin, D. Ausserre, D. Chatenay and T. P. Russell, *J. Phys.*, 1990, **51**, 2801–2811.
76 J. N. L. Albert and T. H. Epps III, *Mater. Today*, 2010, **13**, 24–33.
77 M. Fasolka and A. Mayes, *Annu. Rev. Mater. Res.*, 2001, **31**, 323–355.
78 R. A. Mickiewicz, J. K. W. Yang, A. F. Hannon, Y. Jung, A. Alexander-Katz, K. K. Berggren and C. A. Ross, *Macromolecules*, 2010, **43**, 8290–8295.
79 A. Alexander-Katz, A. G. Moreira and G. H. Fredrickson, *J. Chem. Phys.*, 2003, **118**, 9030–9036.
80 G. Fredrickson, *The Equilibrium Theory of Inhomogeneous Polymers*, Oxford University Press, Oxford, New York, 2005.
81 G. H. Fredrickson, V. Ganesan and F. Drolet, *Macromolecules*, 2002, **35**, 16–39.
82 E. Helfand and Y. Tagami, *J. Chem. Phys.*, 1972, **56**, 3592–3601.
83 T. Hashimoto, M. Shibayama and K. Hiromichi, *Macromolecules*, 1983, **16**, 1093–1101.
84 M. Müller and F. Schmid, *Adv. Polym. Sci.*, 2005, **185**, 1–58.
85 T. P. Lodge, K. J. Hanley, B. Pudil and V. Alahapperuma, *Macromolecules*, 2003, **36**, 816–822.
86 C. Lai, W. B. Russel and R. A. Register, *Macromolecules*, 2002, **35**, 4044–4049.
87 J. Kennemur, L. Yao, F. Bates and M. Hillmyer, *Macromolecules*, 2014, **47**, 1411–1418.
88 A. Alexander-Katz and G. H. Fredrickson, *Macromolecules*, 2007, **40**, 4075–4087.
89 N. Politakos, E. Ntoukas, A. Avgeropoulos, V. Krikorian, B. D. Pate, E. L. Thomas and R. M. Hill, *J. Polym. Sci., Part B: Polym. Phys.*, 2009, **47**, 2419–2427.
90 W. Li, M. Liu, F. Qiu and A.-C. Shi, *J. Phys. Chem. B*, 2013, **117**, 5280–5288.